



Stability analysis of electro-osmotic flow in a rotating microchannel

G.C. Shit^{1,†}, A. Sengupta¹ and Pranab K. Mondal²

¹Department of Mathematics, Jadavpur University, Kolkata 700032, India

²Microfluidics and Microscale Transport Processes Laboratory, Department of Mechanical Engineering, Indian Institute of Technology Guwahati, Guwahati 781039, India

(Received 27 September 2023; revised 4 January 2024; accepted 11 February 2024)

We investigate the linear stability analysis of rotating electro-osmotic flow in confined and unconfined configurations by appealing to the Debye–Hückel approximation. Pertaining to flow in confined and unconfined domains, the stability equations are solved using the Galerkin method to obtain the stability picture. Both qualitative and quantitative aspects of Ekman spirals are examined in stable and unstable scenarios within the unconfined domain. Within the confined domain, the variation of the real growth rate and the transition to instability are analysed using the modified Routh–Hurwitz criteria, employed for the first time in this context. The stability of the underlying flow, characterized by the number of roots with a positive real part, is determined by establishing a Routhian table. The inferences of this analysis show that the velocity plane produces intriguing closed Ekman spirals, which diminish in size with an increase in the rotation speed ω . The Ekman spirals in the stable region exhibit a distinct discontinuity, indicating the dissipation of disturbances over time. In the confined domain, the flow appears consistently stable for a set of involved parameters pertinent to this analysis, such as electrokinetic parameter $K = 1.5$ and rotational parameter ω approximately up to 6. However, the flow instabilities become evident for $K = 1.5$ and $\omega \geq 6$.

Key words: instability control, rotating flows, microfluidics

1. Introduction

The electro-osmotic effect brings in precise control over the underlying flow of small liquid volumes in various miniaturized applications, including lab-on-a-chip devices, microfluidic sensors, bioanalytical systems, microbiological sensors, microelectro-mechanical systems, and many more (Lyklema 1995; Long, Stone & Ajdari 1999; Ghosal 2002; Bahga, Vinogradova & Bazant 2010; Nam *et al.* 2015). It may be mentioned here

[†] Email address for correspondence: gcsnit@jadavpuruniversity.in

that the electro-osmotic effect facilitates the flow control, requiring a lesser energy budget, while realizing this actuation parameter in practice does not involve the cumbersome system to be integrated with the small-scale fluidic circuit/device (Brask, Goranovic & Bruus 2003; Brask *et al.* 2005). Kemery, Steehler & Bohn (1998) have conducted extensive research efforts to investigate several facets of electro-osmotic flow in different microfluidic configurations, encompassing diverse physical and geometric conditions. To this end, a number of experiments have also been conducted by leveraging electro-osmotic effects in centrifugal microfluidic systems, typically in the multiple enzymatic assays (Duffy *et al.* 1999).

It is worth mentioning here that pertaining to rotational flows in lab-on-a-chip-based centrifugal microfluidic systems/devices, used largely in medical diagnostics, biochemical analysis and laboratory instruments cooling, the deployment of electro-osmotic effect offers a few distinctive features, namely noise-free operation, minimally invasive actuation process, and a greater degree of flow controllability, to name a few (Ajdari 1995, 1996; Chakraborty 2006; Mondal *et al.* 2013; Barimani, Jamei & Abbasi 2022). Despite having such inevitable beneficial aspects of the electro-osmotic effect, employment of this flow actuation parameter in rotational platforms leads to a few problematic facets, including a stability issue of the underlying flow (Zhang *et al.* 2013). Probing into the stability threshold of rotational flows in the presence of electrokinetic actuation seems to be of vital importance, attributed primarily to many implications of this characteristic feature on the prevailing transport (Chang & Wang 2011). As witnessed in the reported observations by Posner & Santiago (2006), the onset of instability in rotational force-modulated microscale flows under electrokinetic influences promotes solute mixing quite promisingly. Nevertheless, in electro-osmotic flow, the transition to instability in many cases severely disturbs the underlying transport in the rotating platform, and at times becomes vulnerable for the efficient operation of rotational fluidic systems typically used in biochemical/biomedical applications (Song *et al.* 2017; Sengupta *et al.* 2019). It may be mentioned here that a few studies are reported in the literature wherein the influence of the electro-osmotic effect on the stability picture of non-rotating microscale flows has been discussed aptly (Suresh & Homay 2004; Ray *et al.* 2012).

A substantial application of electrokinetically assisted rotational flow in different state-of-the-art systems, together with the basic interest of unravelling the intricate behaviour of the electro-osmotic effect in triggering instability of rotational flows, indeed, demands a comprehensive stability analysis of rotating electro-osmotic flows. For rotating systems, in addition to the forcing due to the centrifugal effect, the Coriolis force alters the flow velocity, and consequently the fluid flux, considerably (Kaushik *et al.* 2019; Siva *et al.* 2020). Specifically, rotation-induced forcing, i.e. centrifugal force and the Coriolis force, plays a significant role in shaping the flow dynamics (Kaushik, Mondal & Chakraborty 2017b; Gandharv & Kaushik 2022). The underlying effect, influenced by the electrical double layer phenomenon, affects the flow dynamics non-trivially, including the onset of flow instability through the formation of vortices (Abhimanyu *et al.* 2016). Considering all the aspects above, stability analysis of rotating electro-osmotic flow could be an interesting yet practical proposition, which remains unexplored in the literature until the present work.

Here, we consider the effect of channel rotation on the stability analysis of electro-osmotic flow under the influence of electrical forcing that stems from the electrical double layer effect. Our analysis pertains to the framework of the Debye–Hückel approximation, while the validity of this approximation is justified by invoking the relation between surface charge density (σ) and the zeta potential (ζ) (Ganchenko *et al.* 2015).

We consider a dilute aqueous solution of symmetric electrolyte in order to neglect the Joule heating effect from the underlying stability analysis of this work (Mayur, Amiroudine & Lasseux 2012). We perform the stability analysis for the flow over a single plate (unbounded domain) and the flow bounded by two parallel plates using the Galerkin approximation (Reza & Gupta 2012). Quite notably, for the first time, we establish as well as use the modified Routh–Hurwitz criteria (Anagnost & Desoer 1991) to investigate the transition of the flow from stability to instability modes. We mention briefly here that the Routh–Hurwitz criteria serve as a mathematical test to determine the signs of the real parts of the zeros of a polynomial. In § 3.2.2 of this paper, this criterion is utilized to verify analytically the stability of the flow for a specific range of electrokinetic parameter K and rotation number ω . By employing the Routh–Hurwitz criteria, a thorough assessment of the flow stability is achieved, validating the numerical results with analytically verified solutions.

2. Mathematical model and flow configuration

We consider the electro-osmotic flow of an incompressible viscous fluid under the influence of rotation-induced forces through two different configurations, depicted in figure 1. We consider the Cartesian coordinates (x', y', z') to represent the flow configurations, as shown schematically in figure 1. The velocity field $\mathbf{u}' = (u', v')$ is taken along the x' – y' plane. We assume that the entire system rotates along the z' -axis with angular velocity $\boldsymbol{\Omega} = (0, 0, \Omega)$. The external electric field, which is applied along the x' -direction, together with the rotational forcing, drives the flow in the positive x' -axis. For both configurations, we consider height along the z' -axis, width along the y' -axis, and the length spans the x' -axis.

The transport equations governing the electro-osmotic flow dynamics are the Poisson–Boltzmann equation for the potential distribution and the Navier–Stokes system of equations for the flow field.

Let Ψ be the potential distribution due to the electrical double layer (EDL). The EDL potential is governed by the Poisson–Boltzmann equation (Gouy 1910; Chapman 1913; Probst 2005)

$$\frac{d^2\Psi}{dz'^2} = \frac{-\rho_e}{\epsilon}, \tag{2.1}$$

where ϵ is the electrical permittivity of the electrolyte solution under consideration, and ρ_e is the net charge density. Note that $\rho_e = 2C_0ez \sinh(ez\Psi/K_B T)$, where e is the fundamental electric charge, C_0 is the concentration of the bulk electrolyte, z is the valency of ions, K_B represents Boltzmann’s constant, and T is the absolute temperature. Substituting the expression for ρ_e in (2.1), we obtain the equation for EDL potential as

$$\frac{d^2\Psi}{dz'^2} = 2zeC_0 \sinh\left(\frac{ze\Psi}{K_B T}\right). \tag{2.2}$$

For $ze\Psi/K_B T \ll 1$, one may write $\sinh(ze\Psi/K_B T) \approx ze\Psi/K_B T$, and this approximation is known as the Debye–Hückel approximation. Considering the surface charge density for glass ($\sigma = 10^{-3} \text{ C m}^{-2}$), the Gouy–Chapman relation between surface charge density and zeta potential is given by the relation $\sigma = 2\sqrt{2}\epsilon\hat{\phi}/k^{-1} \sinh(\zeta/2\hat{\phi})$ (Ganchenko *et al.* 2015; Demekhin *et al.* 2016). The calculation of ζ from the above relation for $k^{-1} = 200 \text{ nm}$ and $\hat{\phi} = 25 \text{ mV}$ gives the value $\zeta = 0.012 \text{ mV}$ ($\ll 25 \text{ mV}$). As is evident,

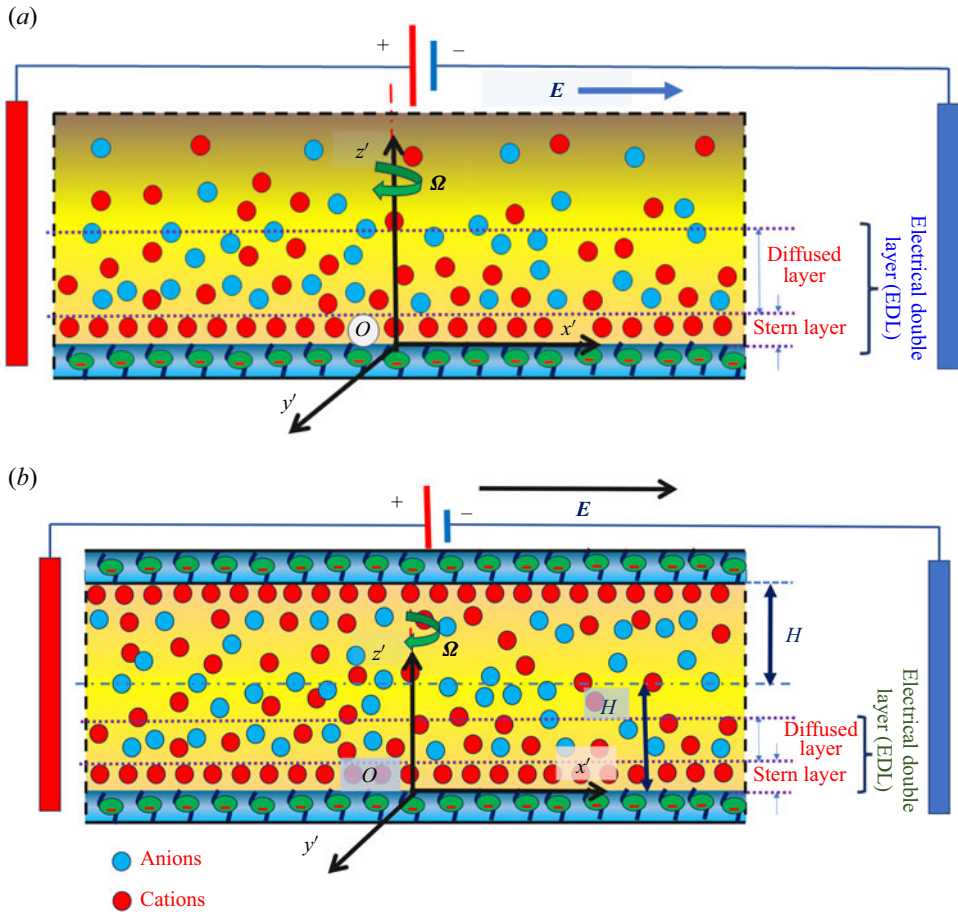


Figure 1. Schematic diagram depicting the geometry of the electro-osmotic flow (a) over a flat infinite plate and (b) in a region bounded by two parallel plates. The external electric field E is being applied along the x' -direction. The entire system is being rotated about the vertical axis, i.e. the z' -axis.

the calculated value of ζ is considerably less than the threshold value of the zeta potential. This order analysis underscores the applicability of the Debye–Hückel approximation pertaining to the present analysis (Masliyah & Bhattacharjee 2006).

By appealing to the Debye–Hückel approximation, we have the following equation that describes the potential, derived from (2.2):

$$\frac{d^2\psi}{dz'^2} = \kappa^2\psi, \quad (2.3)$$

where κ denotes the inverse Debye length, defined by $\kappa = \sqrt{2z^2e^2C_0/\epsilon K_B T}$. Equation (2.3) can be solved subject to the boundary conditions

$$\psi = \zeta \text{ at } z' = 0 \quad \text{and} \quad \psi \rightarrow 0 \text{ as } z' \rightarrow \infty, \quad (2.4a,b)$$

where ζ is the zeta potential at the solid surface.

The Navier–Stokes equations and the equation of continuity for an incompressible fluid flow are written as

$$\rho \left(\frac{\partial \mathbf{u}'}{\partial t'} + \mathbf{u}' \cdot \nabla \mathbf{u}' + 2\boldsymbol{\Omega} \times \mathbf{u}' \right) = \mathbf{f} - \nabla P + \mu \nabla^2 \mathbf{u}', \quad (2.5)$$

$$\nabla \cdot \mathbf{u}' = 0, \quad (2.6)$$

where ρ is the fluid density, μ is the dynamic viscosity, \mathbf{u}' is the velocity vector, \mathbf{f} is the body force, and $P = p - \rho/2|\boldsymbol{\Omega} \times \mathbf{r}'|^2$, with $\mathbf{r}' = (x', y', z')$ the modified pressure (Zheng & Jian 2018). We assume that no pressure gradient exists other than the centrifugal force. The body force for the flow is given by

$$\mathbf{f} = (-\rho_e E, 0, 0), \quad \text{with } \rho_e = -\epsilon \frac{d^2 \Psi}{dz'^2}, \quad (2.7)$$

where ρ_e is the charge density of the electrolyte solution, and E is the constant electric field being applied along the x' -direction. For an infinite plate, one may consider solutions in the form $u' = u'(z', t')$ and $v' = v'(z', t')$. In this analysis, we investigate the stability analysis of purely electro-osmotic flow, and we do not consider any applied pressure gradients in the chosen configuration. However, the prevailing centrifugal forcing owing to the channel rotation develops a pressure gradient in the flow field, and this has been considered in the modified pressure gradient term that acts along the axial (x') direction. The axial pressure gradient, which is assumed to be almost constant across a long microchannel, has also been ignored, considering its minuscule effect in comparison to the electrical forcing. We have considered the width of the channel to be large (pseudo-two-dimensional analysis – here, we did not consider the confinement effect), and the Coriolis force modulated induced pressure gradient along the y' -axis is trivially small. As such, it is because of this small induced pressure gradient along the y' -axis that we did not consider induced pressure gradient along the z' -axis as well. Accounting for these assumptions, which have been considered in seminal works of this paradigm (Kaushik, Mandal & Chakraborty 2017a; Kaushik *et al.* 2019), we did not consider induced pressure gradients along the y' - and z' -directions of this analysis. Consequently, the solution for the velocity components u' and v' (induced due to the Coriolis force) in the long microchannel has been sought to be dependent on z' and t' . Consistent with the assumptions made in this analysis, and by neglecting the convective and pressure gradient terms, the componentwise momentum transport equations obtained from (2.5) read as

$$\rho \frac{\partial u'}{\partial t'} - 2\rho\Omega v' = \epsilon E \frac{d^2 \Psi}{dz'^2} + \mu \frac{d^2 u'}{dz'^2}, \quad (2.8)$$

$$\rho \frac{\partial v'}{\partial t'} + 2\rho\Omega u' = \mu \frac{d^2 v'}{dz'^2}, \quad (2.9)$$

with the boundary conditions given as

$$\mathbf{u}' = 0 \quad \text{at } z' = 0 \text{ and } z' \rightarrow \infty. \quad (2.10)$$

It is worth mentioning here that upon neglecting the electrical body force in the momentum transport equation, the effect that arises due to the formation of the EDL phenomenon can be taken into account through the employment of the Helmholtz–Smoluchowski slip velocity at the wall. Such a consideration is valid only

in the limit of thin EDL cases (Bahga *et al.* 2010). Our study employs a generic approach, i.e. incorporation of the electrical body force in the transport equation (2.8), suitable for both thin and thick EDL scenarios. We justify this approach by noting that surface hydrophobicity boosts electro-osmotic flow, typically modelled through the implementation of a Navier-slip boundary condition at the fluid–solid interface. Past research has shown that uncharged hydrophobic patches on channel walls can intensify electro-osmotic flow velocity, emphasizing the role of the Navier-slip condition in enhancing flow velocity (Bahga *et al.* 2010; Zhao 2010; Belyaev & Vinogradova 2011; Dehe *et al.* 2020). Also, it is evident from the literature that surface charge significantly reduces the hydrophobicity on that particular portion of the wall due to the mobile ions (Ajdari & Bocquet 2006; Maduar *et al.* 2015; Xie *et al.* 2020). In this analysis, we consider a uniformly charged wall, and the maximum value of slip length on such a uniformly charged wall would be approximately 40 nm (Xie *et al.* 2020), leading to an overall enhancement of electro-osmotic flow velocity by a factor $(1 + 40\kappa)$, where κ is the inverse of the EDL thickness in nm. Pertaining to this analysis, κ^{-1} or $\lambda_D = 200$ nm, hence the slip-modulated velocity enhancement factor becomes 1.2. Accounting for this trivial enhancement factor of electro-osmotic flow velocity, we did not consider slip velocity on the surface in the underlying analysis.

3. Analysis of rotating electro-osmotic flow

3.1. Flow dynamics and stability in an unbounded domain

3.1.1. Dimensionless equations

We make an effort to cast (2.3), (2.5) and (2.6) into their dimensionless counterparts. Normalizing lengths by $1/\kappa$, Ψ by ζ , the velocity components by $\epsilon E\zeta/\mu$, and time by $\rho/\mu\kappa^2$, we obtain the dimensionless forms of (2.3), (2.8) and (2.9) as

$$\frac{\partial^2 \psi}{\partial z^2} = \psi, \tag{3.1}$$

$$\frac{\partial^2 u}{\partial z^2} - \frac{\partial u}{\partial t} + 2 \frac{Re}{Ro} v = - \frac{\partial^2 \psi}{\partial z^2}, \tag{3.2}$$

$$\frac{\partial^2 v}{\partial z^2} - \frac{\partial v}{\partial t} - 2 \frac{Re}{Ro} u = 0. \tag{3.3}$$

The dimensionless numbers appearing in (3.2) and (3.3) are $Re = U_0\rho/\kappa\mu$, the Reynolds number, and $Ro = U_0\kappa/\Omega$, known as the Rossby number (Aurnou, Horn & Julien 2020). The term U_0 appearing in the definitions of Re and Ro is called the Helmholtz–Smoluchowski velocity.

Using the boundary conditions $\psi(0) = 1$ and $\psi(\infty) = 0$ for the dimensionless EDL potential ψ , the solution to (3.1) has the form

$$\psi = e^{-z}. \tag{3.4}$$

The following boundary conditions govern the flow field:

$$\mathbf{u} = \mathbf{0} \text{ at } z = 0 \quad \text{and} \quad \mathbf{u} \rightarrow \mathbf{0} \text{ when } z \rightarrow \infty. \tag{3.5}$$

3.1.2. Linear stability analysis

We consider the solutions of (3.2) and (3.3) in the form (Chandrasekhar 2013)

$$\begin{bmatrix} u(z, t) \\ v(z, t) \\ \psi(z, t) \end{bmatrix} = \begin{bmatrix} \hat{u}(z) \\ \hat{v}(z) \\ \hat{\psi}(z) \end{bmatrix} \exp(i\alpha z - \beta t), \tag{3.6}$$

where \hat{u} , \hat{v} and $\hat{\psi}$ respectively denote the amplitudes of velocities and dimensionless EDL potential. Here, α is the wavenumber along the z -direction, and β is the complex growth rate. Henceforth, the ‘hat’ (^) symbol has been omitted from the dimensionless variables for ease of presentation.

On substituting (3.6) into (3.2) and (3.3), we obtain the equations

$$\psi'' + 2i\alpha\psi' - (\alpha^2 + 1)\psi = 0, \tag{3.7}$$

$$u'' + 2i\alpha u' + (\beta - \alpha^2)u + 2\omega v + \psi = 0, \tag{3.8}$$

$$v'' + 2i\alpha v' + (\beta - \alpha^2)v - 2\omega u = 0. \tag{3.9}$$

Here, the prime (') represents the derivative with respect to z . We denote $\omega = \eta^2 = \Omega\rho/\kappa^2\mu = Re/Ro$, where the parameter η is defined as the measure of the thickness of EDL relative to the depth of the Ekman layer. Precisely, we have $\eta = \lambda_D/L_k$, where λ_D is the Debye length, and $L_k (= (\mu/\rho\Omega)^{1/2})$ is defined as the Ekman depth (Chang & Wang 2011).

Let us take $\chi(z) = \hat{u}(z) + i\hat{v}(z)$, where χ is defined as the complex velocity function. By using this complex velocity function χ in (3.8) and (3.9), we get the equation

$$\chi'' + 2i\alpha\chi' + m^2\chi = 0, \tag{3.10}$$

where $m^2 = \beta - \alpha^2 - 2i\omega$.

The boundary conditions used for solving (3.10) are

$$\chi(0) = 0 \quad \text{and} \quad \chi(\infty) = 0, \tag{3.11a,b}$$

and

$$\psi(0) = 1 \quad \text{and} \quad \psi(\infty) = 0. \tag{3.12a,b}$$

Now the solution of (3.10) subject to the boundary conditions described in (3.11a,b) is obtained as

$$\chi = \frac{1}{1 - p + m^2} \left(\exp\left(-z/2\left(p + \sqrt{-4m^2 + p^2}\right)\right) - \exp(-z) \right). \tag{3.13}$$

3.1.3. Generalized flow analysis

In order to investigate the general flow analysis, we first resolve χ into its real and imaginary parts:

$$\hat{u} = \text{Re}(\chi) = \frac{e^{-az} (\cos(bz) (1 + \beta - \alpha^2) + 2(\alpha + \omega) \sin(bz)) - e^{-z} (1 + \beta - \alpha^2)}{(1 + \beta - \alpha^2)^2 + 4(\alpha + \omega)^2} \tag{3.14}$$

and

$$\hat{v} = \text{Im}(\chi) = \frac{e^{-az} (2(\alpha + \omega) \cos(bz) - (1 + \beta - \alpha^2) \sin(bz)) - 2(\alpha + \omega) e^{-z}}{(1 + \beta - \alpha^2)^2 + 4(\omega + \alpha)^2}. \tag{3.15}$$

In this context, \hat{u} is called the axial electro-osmotic velocity in the axial direction of the applied external electric field, while \hat{v} is the electro-osmotic flow velocity in the transverse direction. The quantities a and b in (3.14) and (3.15) are defined in the form

$$a = \sqrt{\frac{\beta - \alpha^2 + |m^2|}{2}} \quad \text{and} \quad b = \sqrt{\frac{-(\beta - \alpha^2) + |m^2|}{2}}. \tag{3.16a,b}$$

For $\alpha = 0$ and $\beta = 0$, the Ekman spiral curve coincides with the reported results (Chang & Wang 2011). However, the generalized flow analysis for the case $\beta \neq 0$ is our aim in this work.

3.1.4. Analysis of the Ekman spiral flow by Galerkin approximation

We consider two cases.

Case A: consider $\alpha = 0$ and $\beta = 0$.

It is known that an Ekman spiral refers to wind or current structures that are developed near a horizontal boundary. As one moves away from the boundary region, the direction of the flow deviates from the external forcing and rotates gradually. Generally, the transport of volume associated with the Ekman spiral occurs in the right-hand direction towards the northern hemisphere. However, in the case of electro-osmotic flow, the Ekman spirals exhibit different characteristics. The direction of the volume transportation of electro-osmotic flow is essentially dependent on ω as depicted in figure 2. The Ekman spirals obtained in this scenario are observed as closed curves, and as the value of ω increases, the area enclosed by the curves tends to decrease. Notably, each closed curve originates from the origin ($z = 0$). As z increases, the u -component swirls along the positive x -axis, while the component v swirls along the negative y -axis. When u reaches its maximum value, the spiral changes direction until the $-v$ velocity reaches its maximum. Following this, the magnitudes of both u and v begin to decrease, eventually spiraling back towards the origin as witnessed in figure 2.

We rewrite (3.7) and (3.10) as

$$\psi'' + p\psi' - q\psi = 0 \tag{3.17}$$

and

$$\chi'' + p\chi' + m^2\chi + \psi = 0, \tag{3.18}$$

where $q = \alpha^2 + 1$. Equations (3.17) and (3.18) along with the boundary conditions (3.11a,b) and (3.12a,b) are solved using Galerkin approximation. We approximate the functions $\chi(z)$ and $\psi(z)$ by a finite series that can be obtained from a complete continuous set of linearly independent functions $\chi_n(z)$ and $\psi_n(z)$. The functions are approximated in such a way that they satisfy the boundary conditions. We take the following approximations for χ and ψ :

$$\left. \begin{aligned} \chi(z) &= \sum_{n=1}^N a_n \chi_n(z), \\ \psi(z) &= \sum_{n=1}^N b_n \psi_n(z), \end{aligned} \right\} \tag{3.19}$$

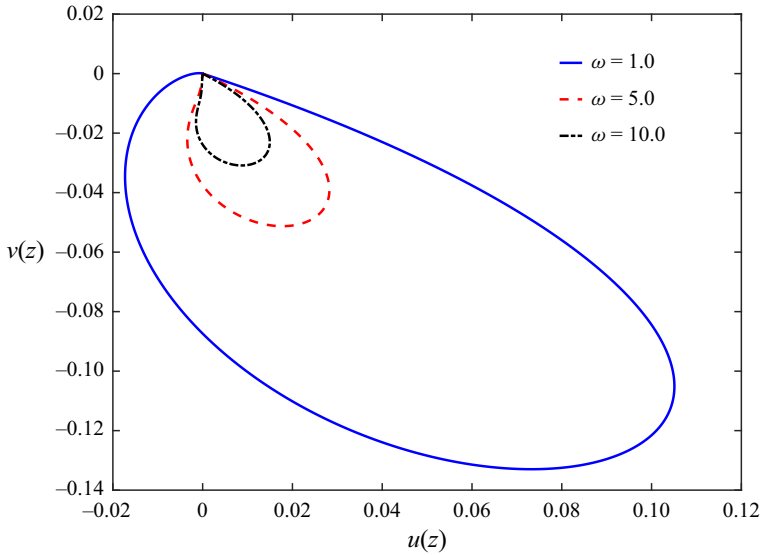


Figure 2. When considering a single plate, the Ekman spirals exhibit different closed spirals in the steady state corresponding to different values of ω . Regardless of the value of ω , closed spirals are obtained consistently. However, as the value of ω increases, the area enclosed by these spirals gradually shrinks in size.

where a_n and b_n are constants. For the sake of mathematical simplicity, we consider $n = 2$ and the following basis functions for $\chi_n(z)$ and $\psi_n(z)$:

$$\chi_1(z) = z e^{-z}, \quad \chi_2(z) = z^2 e^{-z}, \tag{3.20a,b}$$

and

$$\psi_1(z) = e^{-z}, \quad \psi_2(z) = e^{-2z}. \tag{3.21a,b}$$

The relevant equations (3.20a,b) and (3.21a,b) are substituted in (3.17) and (3.18). The residuals are obtained in each case. The sets of coefficients a_n and b_n are determined using the fact that each residual is orthogonal to the set of trial functions over the selected domain. The integral formulation can be written as

$$\int_0^\infty \chi_n(z) R_1 dz = 0 \quad \text{and} \quad \int_0^\infty \psi_n(z) R_2 dz = 0 \quad (n = 1, 2), \tag{3.22a,b}$$

where R_1 and R_2 are the respective residues. Equations (3.22a,b) lead to a homogeneous system of linear equations with four unknowns. The necessary condition for the existence of a non-trivial solution gives rise to the approximated equation

$$0.0016(1.6 + m^4 + 1.32\alpha^2 - 5.33\beta + 5.33\alpha^2 + 10.66i\omega + 4i\alpha\beta - 4i\alpha^3 + 8\alpha\omega) \times (\beta - \alpha^2 - 2i\omega - 2.5\alpha^2 + 0.5\alpha^4 - 3i\alpha + 3i\alpha^3) = 0. \tag{3.23}$$

This equation is solved numerically to obtain the values of α for which the flow is either stable or unstable. Consequently, the nature of the Ekman spirals is analysed in the stable and unstable regions.

Case B: we analyse Ekman spirals in unstable and stable regions.

In the unstable region, the Ekman spirals are closed curves that initiate from the origin. In the unstable region, as the value of ω increases in the range $\omega < 1$, the area enclosed by the Ekman spirals also increases, and the spirals gradually shift towards the left.

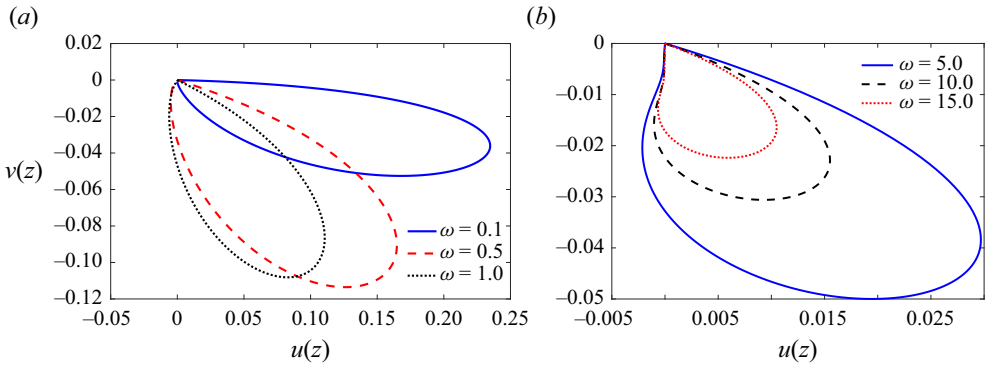


Figure 3. Unstable Ekman spirals: (a) when $\omega \leq 1$, (b) when $\omega > 1$. Closed Ekman spirals initiating from the origin are obtained in unstable cases as well. The deviation of the spirals towards the left is substantially smaller when $\omega > 1$ compared to when $\omega \leq 1$.

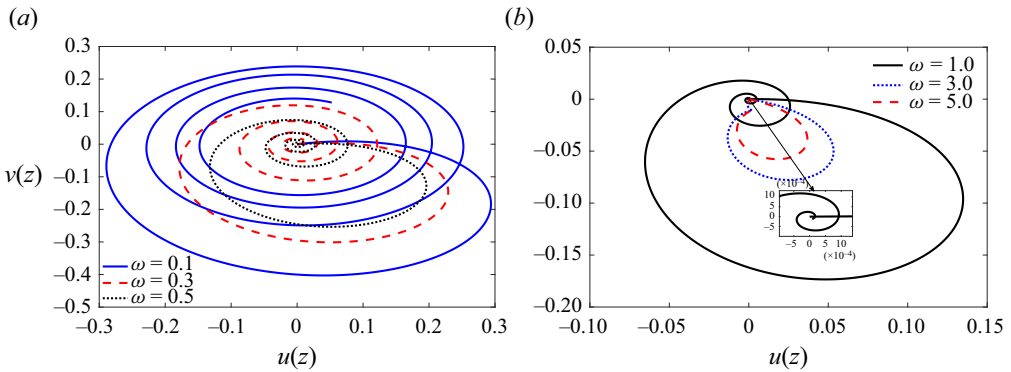


Figure 4. In the case of stable flow, the Ekman spirals are broken curves with the origin as the initiation point. (a) A prominent discontinuity is observed for smaller values of ω . (b) As ω increases, the discontinuity in each Ekman spiral diminishes. For $\omega = 1$, the discontinuity in the Ekman spiral is shown in the inset.

On the other hand, when $\omega > 1$, the Ekman spirals continue to shift towards the left as the value of ω increases. However, the area enclosed by the spirals becomes smaller with increasing values of ω . The maximum enclosed area is obtained at $\omega = 1$. By comparing figures 3(a) and 3(b), it is apparent that the deviation of the Ekman spirals in the leftward direction is considerably smaller for $\omega \geq 1$ compared to $\omega < 1$.

In the stable region (when $\text{Re}(\beta) > 0$), the behaviour of the Ekman spirals differs from that in the unstable region, as can be seen in figure 4. In the stable region, the Ekman spirals appear as broken curves that initiate from the origin. As the value of ω increases, the discontinuity or ‘cut’ present in the broken spiral gradually diminishes, but a closed curve is never formed. Additionally, with an increasing value of ω , the area covered by the curve also reduces, and finally, the discontinuity or ‘cut’ in the spiral moves closer to the origin. As $\omega \rightarrow \infty$, both axial and lateral electro-osmotic flow velocities become negligible. This observation indicates that as $\omega \rightarrow \infty$, the system behaves like a rigid body, where the fluid motion becomes significantly restricted.

3.1.5. Physical significance of the Ekman spirals

We introduce the rotational parameter ω , defined as the ratio of the Reynolds number Re to the Rossby number Ro . A small Rossby number Ro indicates a strong Coriolis force. Given the relationship $\omega = Re/Ro$, the influence of the Coriolis force becomes more dominant compared to the viscous force of the fluid with the increasing values of ω in the regime $\omega > 1$. Consequently, the Ekman spirals become more tightly confined and shrink in size with increasing ω . Conversely, $\omega < 1$ signifies a weaker Coriolis force, and in this regime, the viscous force predominates, resulting in disorganized and shifting spiral patterns. However, in the case of stable flow, where perturbations and disturbances have reduced impact, the Ekman spirals align almost perfectly, as depicted in [figure 4](#).

The Ekman spiral curves obtained in both stable and unstable regions hold physical significance, as the curves arise due to the Coriolis effect. The distinction between ‘complete’ and ‘broken’ Ekman spirals reflects the persistence or decay of disturbances developed owing to the Coriolis force. In the unstable region, the closed curves of the Ekman spirals suggest that the disturbances developed by the Coriolis effect persist indefinitely and spiral along the closed curves. This implies that the influence of the Coriolis force continues to shape the flow patterns in the unstable region. In the stable region, it is observed from [figure 4](#) that the Ekman spirals do not form closed curves and consist of a discontinuity or ‘cut’ near the origin. The extent of discontinuity, equivalently opening of the ‘cut’, reduces in size with the increasing value of ω , as illustrated in [figures 4\(a\)](#) and [4\(b\)](#). This observation signifies that as the value of ω increases, the disturbance being developed also increases. Consequently, the ‘cut’ opening decreases, implying that the disturbances die out beyond a certain period of time.

3.2. Flow dynamics and stability in a bounded domain

Now we consider the flow through a microchannel of height $2H$ bounded between two parallel plates. The electro-osmotic flow of electrolyte solutions is governed by [\(2.8\)](#) and [\(2.9\)](#), while [\(2.3\)](#) governs the electrical potential function. Here, we normalize the lengths by H instead of $1/\kappa$. The dimensionless equation for EDL potential obtained from [\(2.2\)](#) is then given by

$$\frac{\partial^2 \psi}{\partial z^2} = \beta^* \sinh(\alpha^* \psi), \tag{3.24}$$

where $\beta^* = H^2 \kappa^2 / \alpha^*$, and $\alpha^* = ze\zeta / K_B T$. The term α^* is called the ionic energy parameter. For electrolytic systems having low surface zeta potential ($\ll 25\text{mV}$) at 25°C , we have $\alpha^* < 1$ ([Mayur et al. 2014](#)). In such a situation, the Debye–Hückel approximation is applicable, which reduces [\(3.24\)](#) to

$$\frac{\partial^2 \psi}{\partial z^2} = K^2 \psi, \tag{3.25}$$

where $K = \kappa H$ is said to be dimensionless electrokinetic width, also known as the electro-osmotic parameter. The normalized momentum transport equations are

$$\frac{\partial^2 u}{\partial z^2} - \frac{\partial u}{\partial t} + 2\omega v = -\frac{\partial^2 \psi}{\partial z^2}, \tag{3.26}$$

$$\frac{\partial^2 v}{\partial z^2} - \frac{\partial v}{\partial t} - 2\omega u = 0, \tag{3.27}$$

where $\omega = Re/Ro = \Omega H^2 \rho / \mu$, and $Re = \rho U_0 H / \mu$, $Ro = U_0 / \Omega H$. Here, we define ω as a dimensionless parameter known as the rotational Reynolds number (Murthy 1987). In this analysis, Ω is not dependent on the EDL thickness but is a measure of fluid transport due to a rotation by virtue of the viscous effect.

For the analysis, we have assumed specific ranges of pertinent parameters: $\omega = 0.1, 1.0, 10$, and $K = 1.5, 10, 20$. These values were chosen based on the physical properties of the electrolyte solution and dimension of the fluidic configuration, such as the channel half-height H , which is taken within the range 500 nm–10 μm , λ_D of the order of 10^2 nm (Dutta & Beskok 2001), and Ω ranging from 100 to 1000 rps. For instance, when H is set at 4 μm , λ_D is set at 200 nm, and Ω varies from 100 to 1000 rps, the corresponding values are calculated as $K = 20$ and $\omega = 10$. Analogously, similar estimations were performed for the other parametric values. It may be mentioned here that for the bounded flow configuration, we consider channel half-height H to define the electrokinetic parameter $K (= \kappa H = H / \lambda_D)$. Theoretically, $K = 1$ is a case signifying the onset of EDL overlap for the present analysis. However, the minimum value of $K (= 1.5)$, as considered in this analysis, suggests that the channel half-height is larger than the EDL thickness. Taking this into account, we opted not to consider the phenomenon of EDL overlapping in this work.

3.2.1. Linear stability analysis

We assume that the normal mode solutions to (3.25), (3.26) and (3.27) are taken in the form

$$\begin{bmatrix} u(z, t) \\ v(z, t) \\ \psi(z, t) \end{bmatrix} = \begin{bmatrix} \hat{u}(z) \\ \hat{v}(z) \\ \hat{\psi}(z) \end{bmatrix} \exp(i\alpha z - \beta t), \tag{3.28}$$

where α is the wavenumber along the z -direction and β is the growth rate (which can be a complex quantity). Substituting these modes into (3.25), (3.26) and (3.27), and considering $\chi = \hat{u} + i\hat{v}$, we obtain the equations

$$\chi'' + a\chi' + b\chi + K^2\psi = 0 \tag{3.29}$$

and

$$\psi'' + a\psi' - L\psi = 0. \tag{3.30}$$

The corresponding boundary conditions are defined as

$$\chi(\pm 1) = 0 \quad \text{and} \quad \psi(\pm 1) = 1, \tag{3.31a,b}$$

where $a = 2i\alpha$, $b = \beta - \alpha^2 - 2i\omega$ and $L = K^2 + \alpha^2$, and we rewrite $\hat{\psi}$ as ψ by dropping the hat symbol.

The relevant equations (3.29) and (3.30), along with the boundary conditions (3.31a,b), are solved using a Galerkin approximation method as adopted in Reza & Gupta (2012) and Shivakumara *et al.* (2012). The functions $\chi(z)$ and $\psi(z)$ are approximated by a finite series obtained from a complete continuous set of linearly independent functions $\chi_n(z)$

and $\psi_n(z)$. We take the following approximate solutions for χ and ψ :

$$\left. \begin{aligned} \chi(z) &= \sum_{n=1}^{n=N} a_n \chi_n(z), \\ \psi(z) &= \sum_{n=1}^{n=N} b_n \psi_n(z), \end{aligned} \right\} \quad (3.32)$$

where a_n and b_n are constants, and $\chi_n(z)$ and $\psi_n(z)$ denote the sets of basis functions satisfying the respective boundary conditions. We choose

$$\chi_1(z) = z(1 - z^2), \quad \chi_2(z) = (1 - z^2)^2 \quad (3.33a,b)$$

and

$$\psi_1(z) = z^4, \quad \psi_2(z) = z^2. \quad (3.34a,b)$$

On substituting the approximated solutions (3.33a,b) and (3.34a,b) into (3.29) and (3.30), residuals are obtained in each case. The sets of coefficients a_n and b_n can be obtained by using the fact that each residual is orthogonal to the set of trial functions over the selected domain. The integral formulation of the Galerkin approximation for $\chi_n(z)$ and $\psi_n(z)$ can be written as

$$\int_{-1}^1 \chi_n(z) R_1 dz = 0, \quad n = 1, 2, \quad (3.35)$$

and

$$\int_{-1}^1 \psi_n(z) R_2 dz = 0, \quad n = 1, 2, \quad (3.36)$$

where R_1 and R_2 are the respective residues.

Equations (3.35) and (3.36) lead to a homogeneous system of linear equations in four unknowns. The necessary condition for the existence of a non-trivial solution gives rise to

$$\begin{vmatrix} -1.6 + 0.152b & -0.609a & 0 & 0 \\ 0.609a & 0.812b - 2.438 & 0.051K^2 & 0.152K^2 \\ 0 & 0 & 3.428 - 0.222L & -0.285L + 0.8 \\ 0 & 0 & 4.8 - 0.285L & 1.33 - 0.4L \end{vmatrix} = 0. \quad (3.37)$$

On expanding (3.37), we obtain the following approximated biquadratic equation in K as

$$\begin{aligned} &L^2(0.0295 + 0.0028a^2 - 0.0126b + 0.0009b^2) - L(0.2673 + 0.0249a^2 - 0.1123b + 0.008b^2) \\ &+ (2.76411 + 0.2628a^2 - 1.1832b + 0.0874b^2) = 0, \end{aligned} \quad (3.38)$$

where K is the dimensionless electrokinetic width, $a = 2i\alpha$, $b = \beta - \alpha^2 - 2i\omega$ and $L = K^2 + \alpha^2$. Equation (3.38) consists of both real and imaginary parts. However, the physical definition of K requires that K must be real. Hence the solution of (3.38) for a fixed value of ω is considered by taking the absolute value of K . This consideration is valid because in (3.29), $\chi = \hat{u} + i\hat{v}$ represents complex velocity potential. The plot of $|K|$ versus α , as depicted in figure 5(a), illustrates the neutral stability curve with respect to the parameter K for the complex velocity potential. As $\beta = \beta_r + i\beta_i$, we consider the case of direct bifurcation when $\beta_r = \beta_i = 0$. In this situation, (3.38) can be solved to get the neutral curve with respect to the parameter K for complex velocity potential with different

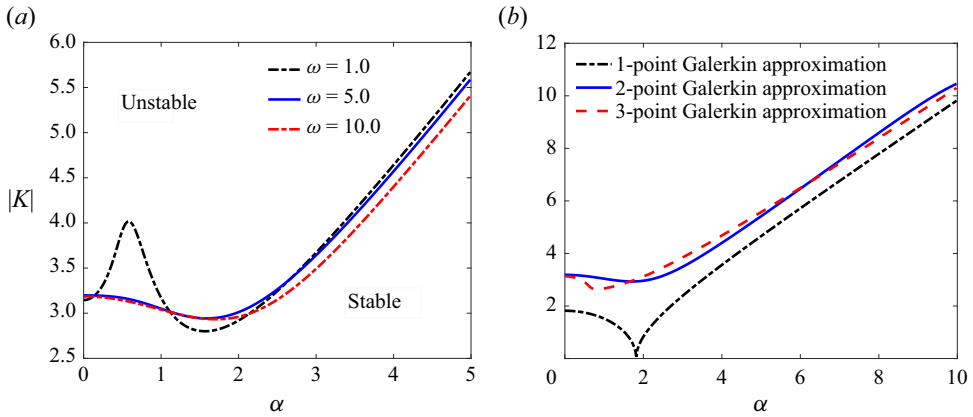


Figure 5. (a) Neutral stability curve for K versus α with different values of ω . The neutral stability curve separates the regions of stability and instability of fluid flow. In this illustration, the stable region exhibits on the lower side of each neutral stability curve, while the upper side corresponds to the unstable region. As the value of ω increases, the instability region increases. (b) Comparison of the numerical results by taking a singular-term Galerkin approximation, a two-point Galerkin approximation and a three-point Galerkin approximation when $\omega = 10$.

values of ω . From figure 5(a), we observe that with an increase in ω , the regions of both stable and unstable zones change significantly. To ascertain the accuracy of our results, we conducted analyses using one, two and three basis functions within the Galerkin expansion framework. Our findings indicate that the outcomes derived from employing two and three basis functions are closely aligned. However, as witnessed in figure 5(b), there is a noticeable discrepancy in the results when considering only a singular term in the Galerkin approximation. A comparative illustration of these results is presented in figure 5(b). While the inclusion of three basis functions provides rigorous insights, the associated computational complexities prompted us to utilize a more streamlined approach with two basis functions for the present analysis.

Figures 6(a) and 6(b) plot the variation of real growth rate β_r versus wavenumber α for different values of K , obtained at $\omega = 1$ and 10, respectively. It is worth mentioning that pertaining to the case $\omega = 1$, no instability is observed for $K = 1.5$. This observed behaviour can be attributed to a relatively lower strength of rotational forcing for $\omega = 1$ together with a significantly smaller electrokinetic parameter at $K = 1.5$. However, as the value of K increases, the channel width also increases, leading to the emergence of instabilities beyond a critical wavenumber. The critical wavenumber, which corresponds to a zero growth rate, can be calculated by identifying the value of α at which the growth rate becomes zero, as indicated by the curve. As witnessed in figures 6(a) and 6(b), for $\omega = 1$ and higher values of K , the flow remains stable for smaller values of α . However, instabilities start to manifest as the wavenumber increases. These inferences suggest that the stability of the underlying flow is influenced by the rotation parameter (ω) and the electrokinetic width (K), leading to a wider range of wavenumbers implicating the onset of instabilities.

In the analysis dealing with the transition to instability with a fixed value of K and for different values of ω as depicted in figures 6(a) and 6(b), we observe that for $K = 1.5$, the flow remains stable for $\omega = 1$. It can also be shown (as elaborated later) that for $K = 1.5$, the flow remains stable for $\omega \approx 5.95$. This is also depicted in figure 7(a).

Stability analysis of electro-osmotic flow

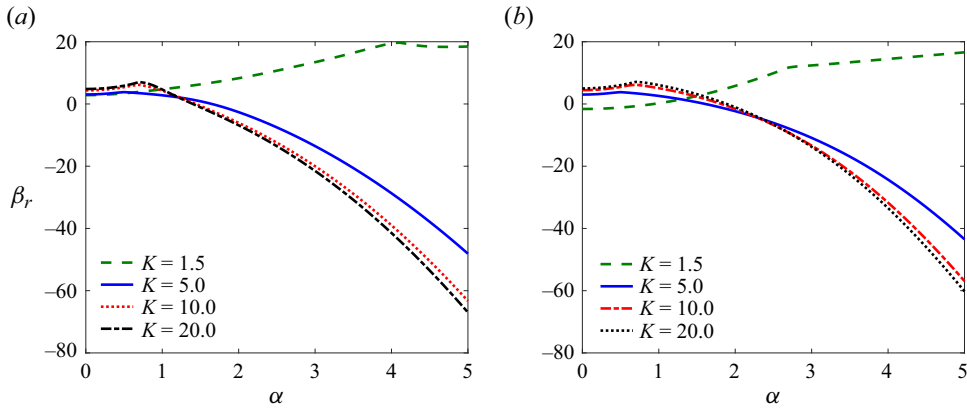


Figure 6. Variation of real growth rate β_r versus α and transition from stability to instability. (a) Different values of K when $\omega = 1$. When $K = 1.5$ and $\omega = 1$, the flow is always stable. This trend of stable flow for $K = 1.5$ continues for a value of ω taken roughly up to 5.95. (b) Different values of K when $\omega = 10$. When K is small, there is a transition towards stability from instability. However, as K is increased, the flow gradually transits to an unstable flow from a stable flow.

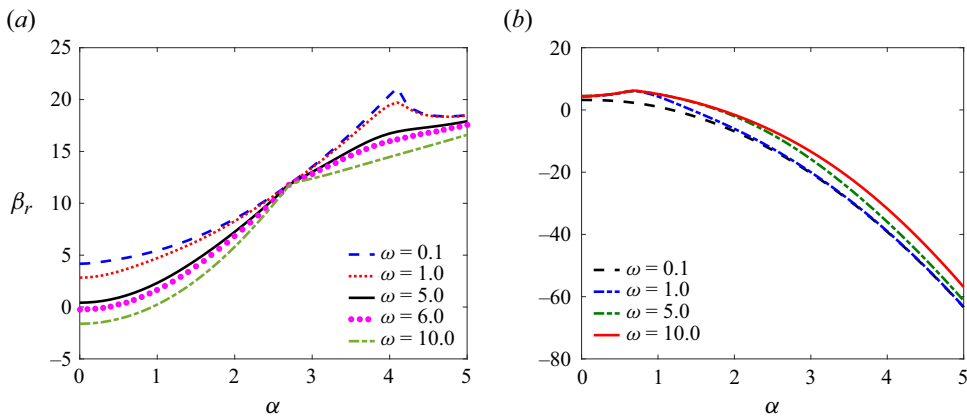


Figure 7. Variation of real growth rate β_r versus α and transition from stability to instability. (a) Different values of ω when $K = 1.5$. For significantly small values of K , the flow gradually tends to be stable with increasing wavenumber. (b) Different values of ω when $K = 10$. For large values of K , the flow is stable only for smaller wavenumbers, while the instabilities occur in the flow as the wavenumber increases.

However, instabilities start to emerge as ω increases beyond its critical value ($\omega \geq 6$). These instabilities gradually lead to stability as the wavenumber increases. This observation suggests a transition from stability to instability as ω exceeds a critical value. The exact critical value of ω depends specifically on the problem under consideration.

Figure 7(b) shows different trends of the stability picture for the higher values of ω considered. At a higher value of ω ($= 10$), the flow is stable only for smaller wavenumber α . Increasing the value of α , the flow gradually becomes unstable, as witnessed by the growth rate curve for different values of K in the figure.

We rewrite (3.38) in the form

$$AK^4 - BK^2 + C = 0, \tag{3.39}$$

where A , B and C are defined in Appendix A.

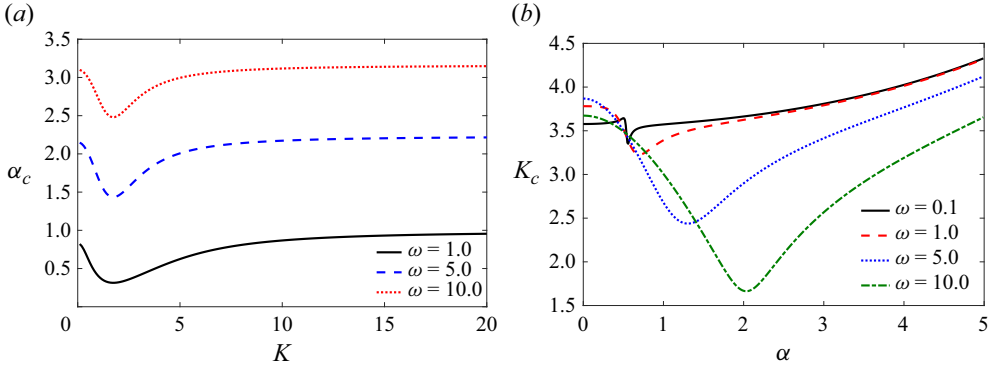


Figure 8. (a) Variation of critical wavenumber α_c with electro-osmotic parameter K , for different values of ω . As ω increases, the critical value of α becomes gradually higher. (b) Variation of critical K with wavenumber at different values of ω .

We seek to find the critical wavenumber above which instabilities appear in the flow corresponding to the different values of K and ω . We put $\beta = 0$ in (3.39), and perform an implicit derivative of K with respect to α^2 . Thus the rate of change of K with respect to α^2 is obtained as

$$\frac{dK}{d\alpha^2} = \frac{\Lambda K^4 + K^2(2\alpha^2\Lambda + 2\delta - \Gamma) + (\alpha^4\Lambda + 2\delta\alpha^2 - \alpha^2\Gamma - \xi + \epsilon)}{4K^3\delta + 2\tau K}, \quad (3.40)$$

where $\tau, \delta, \Lambda, \Gamma, \xi, \epsilon$ are defined in Appendix A. In order to find the critical wavenumber α_c , $dK/d\alpha^2$ is set to zero. As a result, we obtain

$$\Lambda K^4 + K^2(2\alpha_c^2\Lambda + 2\delta - \Gamma) + (\alpha_c^4\Lambda + 2\delta\alpha_c^2 - \alpha_c^2\Gamma - \xi + \epsilon) = 0. \quad (3.41)$$

This equation is solved numerically for different values of ω after substituting the value of K from (3.39). It is to be noted that since wavenumber is a real quantity, only the real part of α_c is to be considered from the solution obtained from (3.41). Finally, the critical wavenumber above which the instabilities appear in the flow can be obtained for different values of K and ω .

In order to study the variation of K_c (critical electro-osmotic parameter) with respect to wavenumber, the reciprocal of (3.40) is set to zero. The expression of K_c for different values of ω as a function of α is thus obtained as

$$K_c = \sqrt{-\frac{\tau}{2\delta}}. \quad (3.42)$$

Figure 8(a) represents the variation of critical wavenumber (α_c) with K for different values of ω . It is seen that with increasing ω , the range of α_c increases. This shows that the system under consideration tends to become stable as ω is increased.

The variation of critical electro-osmotic parameter K_c with wavenumber α for different ω is shown in figure 8(b). It can be seen that with increasing α , the critical electro-osmotic parameter K_c first decreases and then increases with increasing α .

3.2.2. Analytical verification: employment of the modified Routh–Hurwitz criterion

Here, we make an effort to verify the stability threshold of the flow field, employing an analytical method consistent with the modified Routh–Hurwitz criterion. Using this method, we check the stability of the flow for $K = 1.5$ and in the neighbourhood of $\omega = 5.9$. Additionally, we establish by using this method that the flow is always stable for $K = 1.5$ and $\omega \approx 5.95$. The Routh–Hurwitz criterion is a method used to determine whether the real part of a root of an equation is positive or negative. This technique allows us to determine the sign of the real part of the root without solving the equation (D’Azzo & Houpis 1960; Anagnost & Desoer 1991). However, when the equation contains complex coefficients, the standard Routh–Hurwitz criterion is not applicable directly. In such cases, the modified Routh–Hurwitz criterion is employed to analyse the stability of the system (Lung 1966).

Equation (3.38) in terms of β can be expressed as

$$P(\beta) = p\beta^2 - \beta(q + ir) + (x + iy), \tag{3.43}$$

where the terms p, q, r, x, y are given in Appendix B. In order to apply the modified Routh–Hurwitz criterion, we introduce another polynomial $\bar{P}(\beta)$, which is the complex conjugate of the polynomial $P(\beta)$ defined in (3.43). Multiplying (3.43) by its conjugate $\bar{P}(\beta)$, we obtain the polynomial

$$F(\beta) = p^2\beta^4 - 2pq\beta^3 + \beta^2\{2px + (q^2 + r^2)\} - \beta(2qx + 2ry) + (x^2 + y^2). \tag{3.44}$$

As is evident from this equation, the zeros of the above biquadratic polynomial are complex. To determine the nature of the real part of β , which determines the stability of the flow, we construct the Routhian table using (3.44).

The number of sign changes in the first column of the Routhian table corresponds to the number of roots with a positive real part. It is important to note that the number of roots having a positive real part in (3.43) is half the numbers obtained from (3.44).

Using the modified Routh–Hurwitz criterion, we now show that the flow is always stable for $K = 1.5$ and $\omega = 5.9$. If we put $K = 1.5, \omega = 5.9$ in (3.43), then we obtain the polynomial

$$P_{1.5,5.9}(\beta) = 0.1105\beta^2 - \beta(q_1 + ir_1) + (x_1 + iy_1), \tag{3.45}$$

where $q_1 = 1.00028 + 0.211\alpha^2, r_1 = 1.5445, x_1 = -2.0301 + 2.1087\alpha^2 + 0.1106\alpha^4$ and $y_1 = 11.8063 + 2.6091\alpha^2$.

As mentioned earlier, we introduce another polynomial $\overline{P}_{1.5,5.9}(\beta)$, which is the conjugate of $P_{1.5,5.9}(\beta)$, and multiply them to get the resultant biquadratic polynomial

$$F_{1.5,5.9}(\beta) = 0.0122\beta^4 - 0.221q_1\beta^3 + (0.221x + q_1^2 + r_1^2)\beta^2 - (2y_1r_1 + 2q_1x_1)\beta + (x_1^2 + y_1^2). \tag{3.46}$$

Using (3.46), we construct the Routhian table (see table 1a) for $F_{1.5,5.9}(\beta)$.

The expressions A_1, A_2, B_1 and C_1 in table 1(a) are defined in Appendix C.

Based on the analysis of data given in the Routhian table, the values of A_1, A_2, B_1, C_1 are obtained for $\alpha = 0-5$ as given in table 1(b).

By comparing table 1(b) with table 1(a), it is observed that in the Routhian table, there are four changes in sign along the first column. This indicates that the complex polynomial given in (3.46) will have four zeros with a positive real part. This feature, in turn, shows

			α	A_1	A_2	B_1	C_1
0.0112	$0.221x_1 + q_1^2 + r_1^2$	$x_1^2 + y_1^2$	0	1.1488	143.51	-4.80	143.51
-0.221 q_1	$-(2y_1r_1 + 2q_1x_1)$	0	1	1.8856	207.84	-15.24	207.84
A_1	A_2	0	2	4.8290	561.56	-51.08	561.56
B_1	0	0	3	12.1793	1916	-159.98	1916
C_1	0	0	4	27.6035	6470	-475.08	6470
			5	56.2354	20 289	-1282	20 289
(a)			(b)				

Table 1. (a) Routhian table for $F_{1.5,5.9}(\beta)$. (b) Estimation of A_1, A_2, B_1 and C_1 .

0.0112	$0.221m + g^2 + h^2$	$m^2 + n^2$
-0.221 g	$-(2gm + 2hn)$	0
A_1	A_2	0
B_1	0	0
C_1	0	0

Table 2. Routhian table for $F_{1.5,6}(\beta)$.

that the polynomial (3.45) will have two zeros whose real part is positive. Since a positive real β denotes a stable flow, it can be inferred that for $K = 1.5$ and $\omega = 6$, the flow is indeed stable.

Now we aim to show the instabilities in the flow when $K = 1.5$ and $\omega = 6$. We put $K = 1.5$ and $\omega = 6$ in (3.43), yielding the polynomial

$$P_{1.5,6}(\beta) = 0.1105\beta^2 - \beta(g + ih) + (m + in), \tag{3.47}$$

where $g = 1.00028 + 0.2211\alpha^2$, $h = 1.57065$, $m = -2.1793 + 2.2310\alpha^2 + 0.1105\alpha^4$ and $n = 12 + 2.6533\alpha^2$. By introducing the conjugate polynomial, as discussed earlier, and multiplying it with (3.47), we obtain the biquadratic polynomial

$$F_{1.5,6}(\beta) = 0.0122\beta^4 - 0.221\beta^3g + (0.221m + g^2 + h^2)\beta^2 - (2gm + 2hn)\beta + (m^2 + n^2). \tag{3.48}$$

In the Routhian table 2, the expressions for A_1, A_2, B_1, C_1 are the same as defined in table 1.

By constructing a table similar to tables 1(a) and 1(b), and performing an analysis using tabulated data, it is observed that for α in the range 0–0.235, there are two sign changes. This indicates that two zeros of the polynomial (3.48) with a negative real part exist. Consequently, the polynomial (3.47) has one zero whose real part is negative. Therefore, it can be concluded that for $K = 1.5$ and $\omega = 6$, instabilities start to appear in the flow field.

Similarly, using the modified Routh–Hurwitz criterion for different values of K and ω , different ranges of wavenumbers can be obtained at which the flow is unstable.

3.2.3. Generalized flow analysis

Pertaining to the flow in a bounded configuration, we also attempt to demonstrate the flow field as described by the velocity variation in both stable and unstable scenarios.

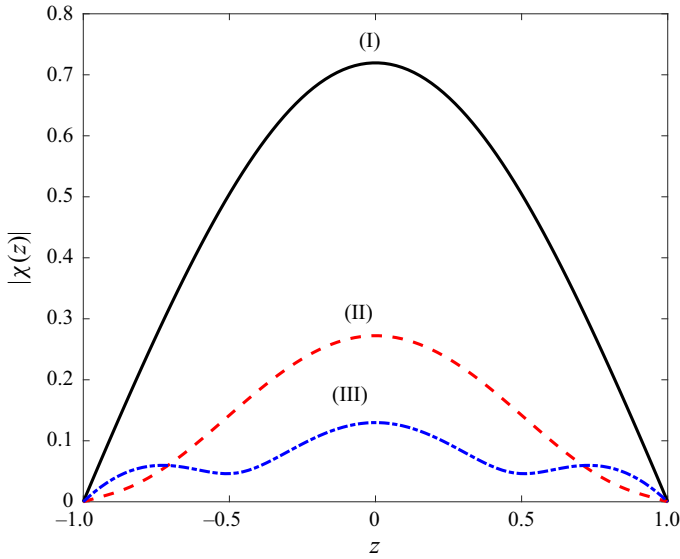


Figure 9. Stable velocity profile of the resultant velocity $|\chi(z)| = \sqrt{(u^2 + v^2)}$ at different wavenumbers and their corresponding growth rate: (I) $\alpha = 0.08$, $\beta = 2.8$; (II) $\alpha = 1.51$, $\beta = 6.37$; (III) $\alpha = 2.48$, $\beta = 10.59$, when $\omega = 1$, $K = 1.5$.

Using (3.25), (3.26) and (3.27), we obtain the differential equation in χ as

$$\chi'' + a\chi' + b\chi = -\frac{K^2 \cosh\{i(\alpha + K)z\}}{\cosh(i\alpha + K)}, \tag{3.49}$$

where $a = 2i\alpha$ and $b = \beta - \alpha^2 - 2i\omega$. The right-hand side of (3.49) is obtained from the analytical solution of (3.25), subject to the boundary conditions of ψ given in (3.31a,b).

The solution of (3.49) using the boundary condition (3.31a,b) takes the form

$$\chi(z) = \frac{e^{i\alpha} K^2}{K^2 - aK + b} \left(\frac{\cosh(lz)}{\cosh l} - \frac{\cosh\{i(\alpha + K)z\}}{\cosh(i\alpha + K)} \right), \tag{3.50}$$

where $l = \sqrt{2i\omega - \beta}$. In particular, the solution for $\alpha = 0$ and $\beta = 0$ reproduces the steady-state solution given by

$$\chi(z) = \frac{K^2}{K^2 - 2i\omega} \left(\frac{\cosh(\sqrt{2i\omega} z)}{\cosh \sqrt{2i\omega}} - \frac{\cosh(Kz)}{\cosh K} \right). \tag{3.51}$$

It is worth mentioning here that the solution described in (3.27) aligns with the findings presented in Chang & Wang (2011). Specifically, for small values of K , the EDL potential reaches a minimum at the centre of the channel. When the value of K is low, the velocity profile of u is approximately parabolic in the absence of rotation, and decreases rapidly with rotation. These observations indicate the influence of rotation on the EDL potential and velocity distribution.

3.2.4. Flow characteristics at stable and unstable regions

The stability of the flow can be assessed by examining the growth rate β . A positive value of β indicates stability, while a negative value signifies flow instability. From figure 9,

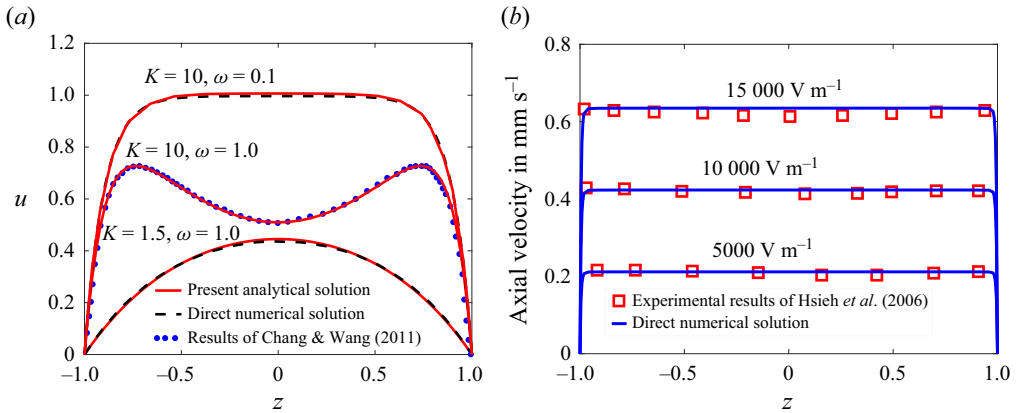


Figure 10. (a) Comparison of axial velocity profiles obtained from the analytical solution at the steady state (when $\alpha = 0$, $\beta = 0$) with direct numerical simulation and previous theoretical investigation. (b) Comparison of the present dimensional axial electro-osmotic flow velocity for the limiting case of zero rotational speed with the experimental results of Hsieh, Lin & Lin (2006) when electro-osmotic mobility is $4.21 \times 10^{-8} \text{ m}^2 (\text{V s})^{-1}$ and zeta potential is -55.32 mV for 10 mM NaCl solution. The dimensional axial velocity is obtained by multiplying the electro-osmotic mobility and electric field into the present dimensionless axial velocity field for the limiting case of zero rotational speed.

we observe that the flow is always stable for $K = 1.5$, $\omega = 1$, hence a fully developed parabolic nature of the velocity profile is obtained. It is also seen that as the wavenumber α and the corresponding growth rate increase, the absolute value of the complex velocity reduces. We have performed full-scale numerical simulations using the finite element framework of COMSOL Multiphysics by considering the Poisson–Boltzmann equation with Gouy–Chapman theory for the description of EDL potential, and the Navier–Stokes equations for a purely electro-osmotically driven flow in a rotating microchannel. The comparison analysis of our results, both analytical solutions and simulated data, with the reported results of Chang & Wang (2011) is presented in figure 10(a). As witnessed in figure 10(a), our analytical solutions agree well with both full-scale simulated and reported theoretical results for all the values of K and ω considered. In figure 10(b), we compare our analytical solutions with the experimental results of Hsieh *et al.* (2006) in the limiting case of a non-rotating channel. It is worth mentioning here that the lack of experimental data pertaining to rotating electro-osmotic flows encouraged us to focus on this benchmarking analysis in the limiting case. The velocity profile in the stability regions is known to expose a fully developed parabolic or wave-like structure. Conversely, in the unstable region, the flow profile takes the form of a flattened parabolic profile as depicted in figure 11(a). Figure 11(a) illustrates the variation of the resultant velocity profile at different stability conditions when the other parameters are $K = 1.5$ and $\omega = 10$, while 11(b) illustrates the resultant velocity profile for $K = 20$ and $\omega = 1$ at different stability conditions. As the value of β increases, the velocity profiles show a plateau-like structure. The disturbance of the flow field occurs near the central line of the channel. For a set of parametric values, i.e. for $K = 1.5$, $\omega = 10$, both least stable and unstable zones exist. The approximate highest negative value of β represents the most unstable velocity profile, while the least stable corresponds to the least positive value of β . The most unstable, as well as least stable, growth rate and its corresponding wavenumbers can be determined from figures 7(a) and 7(b).

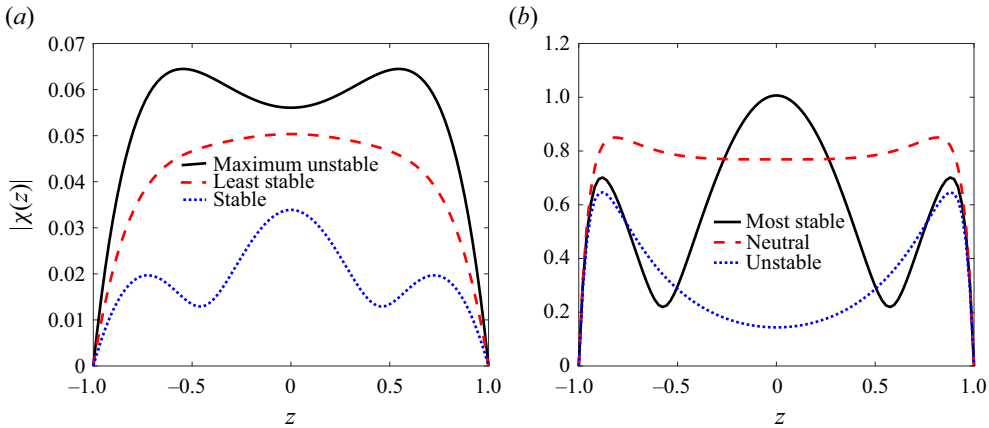


Figure 11. (a) Velocity profile for the electro-osmotic flow $|\chi| = \sqrt{(u^2 + v^2)}$ for $K = 1.5$, $\omega = 10$ when the flow is: maximum unstable ($\alpha = 0.005$, $\beta = -1.613$), least stable ($\alpha = 0.934$, $\beta = 0.0005$) and stable ($\alpha = 2.768$, $\beta = 12$). (b) Velocity profile for the electro-osmotic flow $|\chi| = \sqrt{(u^2 + v^2)}$ for most stable, neutral and unstable regimes when $K = 20$, $\omega = 1$. Here, most stable is defined as a stability of flow with maximum positive growth rate.

These profiles bear significant information about the transition of the field for electro-osmotic flow. This flattening effect can be attributed to the destabilizing factors in the flowing fluid. In the case of instability, the flow velocity profile exhibits a depression or disturbance in the vicinity of the central line of the channel. This depression signifies the disruptive effects of instability on the behaviour of the electro-osmotic flow. This characteristic feature suggests that the flow becomes more turbulent or irregular, deviating from the expected parabolic or wavy shape as demonstrated in stable conditions.

4. Summary, conclusion and perspective

In this work, we present a comprehensive analysis focusing on the stability picture of the rotating electro-osmotic flow in unconfined (single infinite plate) and confined (channel bounded by two parallel plates) configurations. We investigate the transverse flow behaviour in a steady state, and aptly demonstrate its response to varying rotational speeds. Additionally, we perform stability analysis using the semi-analytical framework to explore the velocity profiles in both stable and unstable regions.

For the unconfined case, the present analysis witnesses the presence of closed orbits called Ekman spirals in the plots of axial velocity (u) and lateral velocity (v). As shown in this paper, the size of the Ekman spirals decreases with rotational speed (ω). This behaviour was observed in both steady-state and unstable cases. However, as seen for the unstable case, the spirals are not aligned and shift leftwards with increasing ω . In the stable region, each Ekman spiral is accompanied by a discontinuity, realized by a diminishing cut, indicating the decay of disturbances over time.

Pertaining to the flow in a confined domain, we solve the linear stability equation using the Galerkin approximation method. We depict the neutral stability curves for different values of the electro-osmotic parameter (K) and ω . The results show that the stability of the flow decreased with increasing ω . Applying the modified Routh–Hurwitz criterion, which is employed for the first time in the context of the stability analysis, we establish that the flow was always stable for $K = 1.5$, and ω up to approximately 6. We also undertake

an effort in this work to investigate steady-state flow profiles in both stable and unstable states.

The findings of this paper highlight the significance of both ω and K as crucial parameters in determining the stability of the system. The present modelling framework is deemed pertinent to reveal the effect of time-modulated external electric fields on the stability picture of rotational flows, offering a more practical approach to solve stability issues of the flows in state-of-the-art lab-on-a-chip systems. We believe that the insights gained from the stability analysis of the chosen flow configurations have potential implications in the design and development of various systems, used typically in drug delivery and mass transfer. Moreover, the analysis of the underlying flow, presented in this study, can serve as a basis for investigating solute mixing in annular channels using lateral transverse flow.

Acknowledgements. The authors sincerely thank the esteemed reviewers for their valuable comments and suggestions based on which the present work is improved. The authors would like to acknowledge Dr S.K. Mehta (Research Associate in Microfluidics and Microscale Transport Processes Laboratory, Department of Mechanical Engineering, IIT Guwahati, India) for his help pertaining to COMSOL simulations and graphics.

Funding. This work was supported financially by the Science and Engineering Research Board (SERB), New Delhi (G.C.S., MATRICS Project grant no. MTR/2021/000073) and the UGC, New Delhi for providing a Junior Research Fellowship to A.S.

Declaration of interests. The authors report no conflict of interest.

Data availability statement. The data that support the findings of this study are available within the paper.

Author ORCIDs.

© G.C. Shit <https://orcid.org/0000-0001-6110-2471>;

© Pranab K. Mondal <https://orcid.org/0000-0002-9368-1532>.

Author contributions. G.C.S. and A.S. derived the theory and illustrated results graphically, and P.K.M. performed the simulations. All authors contributed equally to analysing data and reaching conclusions, and in writing the paper.

Appendix A

The terms A , B and C appearing in (3.39) are given by

$$\left. \begin{aligned} A &= 0.0295 + 0.0028a^2 - 0.0126b + 0.0009b^2, \\ B &= 2\alpha^2 A - (0.2673 - 0.09\alpha^2 - 0.1123b + 0.008b^2), \\ C &= \alpha^4 A - \alpha^2(0.2673 - 0.09\alpha^2 - 0.1123b + 0.008b^2) \\ &\quad + (2.7611 - 1.05\alpha^2 - 1.1832b + 0.0874b^2). \end{aligned} \right\} \quad (A1)$$

The terms Λ , Γ , δ , τ , ξ and ϵ in (3.40) and (3.41) are given by

$$\left. \begin{aligned} \Lambda &= -0.0994 + 0.0018\alpha^2 + 0.0036i\omega, \\ \Gamma &= 0.022 + 0.016\alpha^2 + 0.032i\omega, \\ \delta &= 0.0295 - 0.0112\alpha^2 + 0.0126(\alpha^2 + 2i\omega) + 0.0009(\alpha^4 - 4\omega^2 + 4i\alpha^2\omega), \\ \tau &= 2\alpha^2\delta - \{0.2673 - 0.09\alpha^2 + 0.1123(\alpha^2 + 2i\omega) + 0.008(\alpha^4 - 4\omega^2 + 4i\alpha^2\omega)\}, \\ \xi &= \{0.2673 - 0.09\alpha^2 + 0.1123(\alpha^2 + 2i\omega) + 0.008(\alpha^4 - 4\omega^2 + 4i\alpha^2\omega)\}, \\ \epsilon &= 0.1332 + 0.1748\alpha^2 + 0.3496i\omega. \end{aligned} \right\} \quad (A2)$$

Appendix B

The expressions for p , q , r , x and y appearing in (3.43) are defined as

$$\left. \begin{aligned} p &= 0.088 + 0.008K^2 + 0.0009K^4, \\ q &= 1.2 + 0.176\alpha^2 - 0.117K^2 + 0.016\alpha^2K^2 + 0.0126K^4 + 0.0018\alpha^2K^4, \\ r &= 0.352\omega - 0.032\omega K^2 - 0.0036\omega K^4, \\ x &= 2.8056 + 0.136\alpha^2 + 0.088\alpha^4 - 0.0352\omega^2 - 0.274K^2 + 0.928\alpha^2K^2 \\ &\quad + 0.008\alpha^4K^2 - 0.032\omega^2K^2 + 0.029K^4 + 0.0014\alpha^2K^4 \\ &\quad + 0.0009\alpha^4K^4 - 0.0036\omega^2K^4, \\ y &= 2.4\omega + 0.352\alpha^2\omega - 0.234\omega K^2 + 0.032\omega\alpha^2K^2 + 0.0252\omega K^4 + 0.0036\alpha^2\omega K^4. \end{aligned} \right\} \quad (B1)$$

Appendix C

The expressions for A_1 , A_2 , B_1 and C_1 used in table 1 are estimated as

$$\left. \begin{aligned} A_1 &= \frac{1}{-(-0.221q_1)} \begin{vmatrix} 0.0122 & 0.221x_1 + q_1^2 + r_1^2 \\ -0.221q_1 & -(2y_1r_1 + 2q_1x_1) \end{vmatrix}, \\ A_2 &= \frac{1}{-(-0.221q_1)} \begin{vmatrix} 0.0122 & x_1^2 + y_1^2 \\ -0.221q_1 & 0 \end{vmatrix}, \\ B_1 &= \frac{1}{-A_1} \begin{vmatrix} -0.221q_1 & -(2y_1r_1 + 2q_1x_1) \\ A_1 & A_2 \end{vmatrix}, \quad C_1 = \frac{1}{-B_1} \begin{vmatrix} A_1 & A_2 \\ B_1 & 0 \end{vmatrix}. \end{aligned} \right\} \quad (C1)$$

REFERENCES

- ABHIMANYU, P., KAUSHIK, P., MONDAL, P.K. & CHAKRABORTY, S. 2016 Transients in rotational electro-hydrodynamics microflows of a viscoelastic fluid under electrical double layer phenomena. *J. Non-Newtonian Fluid Mech.* **231**, 56–67.
- AJDARI, A. 1995 Electro-osmosis on inhomogeneously charged surfaces. *Phys. Rev. Lett.* **75** (4), 755.
- AJDARI, A. 1996 Generation of transverse fluid currents and forces by an electric field: electro-osmosis on charge-modulated and undulated surfaces. *Phys. Rev. E* **53** (5), 4996.
- AJDARI, A. & BOCQUET, L. 2006 Giant amplification of interfacially driven transport by hydrodynamic slip: diffusio-osmosis and beyond. *Phys. Rev. Lett.* **96** (18), 186102.
- ANAGNOST, J.J. & DESOER, C.A. 1991 An elementary proof of the Routh–Hurwitz stability criterion. *Circ. Syst. Signal Process.* **10** (1), 101–114.
- AURNOU, J.M., HORN, S. & JULIEN, K. 2020 Connections between nonrotating, slowly rotating, and rapidly rotating turbulent convection transport scalings. *Phys. Rev. Res.* **2** (4), 043115.
- BAHGA, S.S., VINOGRADOVA, O.I. & BAZANT, M.Z. 2010 Anisotropic electro-osmotic flow over super-hydrophobic surfaces. *J. Fluid Mech.* **644**, 245–255.
- BARIMANI, M., JAMEI, M.K. & ABBASI, M. 2022 Calculation of electro-osmotic flow development length in a rotating three-dimensional microchannel. *Fluid Dyn. Res.* **54** (5), 055503.
- BELYAEV, A.V. & VINOGRADOVA, O.I. 2011 Electro-osmosis on anisotropic superhydrophobic surfaces. *Phys. Rev. Lett.* **107** (9), 098301.
- BRASK, A., GORANOVIC, G. & BRUUS, H. 2003 Electroosmotic pumping of nonconducting liquids by viscous drag from a secondary conducting liquid. In *Proceedings of the Nanotechnology Conference and Trade Show*, pp. 190–193.
- BRASK, A., GORANOVIC, G., JENSEN, M.J. & BRUUS, H. 2005 A novel electro-osmotic pump design for nonconducting liquids: theoretical analysis of flow rate–pressure characteristics and stability. *J. Micromech. Microengng* **15** (4), 883.

- CHAKRABORTY, S. 2006 Augmentation of peristaltic microflows through electro-osmotic mechanisms. *J. Phys. D: Appl. Phys.* **39** (24), 5356.
- CHANDRASEKHAR, S. 2013 *Hydrodynamic and Hydromagnetic Stability*. Courier Corporation.
- CHANG, C.C. & WANG, C.Y. 2011 Rotating electro-osmotic flow over a plate or between two plates. *Phys. Rev. E* **84** (5), 056320.
- CHAPMAN, D.L. 1913 LI. A contribution to the theory of electrocapillarity. *Lond. Edinb. Dublin Phil. Mag. J. Sci.* **25** (148), 475–481.
- D'AZZO, J.J. & HOUPIS, C.H. 1960 *Feedback Control System Analysis and Synthesis*. McGraw-Hill.
- DEHE, S., ROFMAN, B., BERCOVICI, M. & HARDT, S. 2020 Electro-osmotic flow enhancement over superhydrophobic surfaces. *Phys. Rev. Fluids* **5** (5), 053701.
- DEMEKHIN, E.A., GANCHENKO, G.S., NAVARKAR, A. & AMIROUDINE, S. 2016 The stability of two layer dielectric-electrolyte micro-flow subjected to an external electric field. *Phys. Fluids* **28** (9), 092003.
- DUFFY, D.C., GILLIS, H.L., LIN, J., SHEPPARD, N.F. & KELLOGG, G.J. 1999 Microfabricated centrifugal microfluidic systems: characterization and multiple enzymatic assays. *Anal. Chem.* **71** (20), 4669–4678.
- DUTTA, P. & BESKOK, A. 2001 Analytical solution of time periodic electroosmotic flows: analogies to Stokes' second problem. *Anal. Chem.* **73** (21), 5097–5102.
- GANCHENKO, G.S., DEMEKHIN, E.A., MAYUR, M. & AMIROUDINE, S. 2015 Electrokinetic instability of liquid micro- and nanoflows with a mobile charge. *Phys. Fluids* **27**, 062002.
- GANDHARV, S. & KAUSHIK, P. 2022 Transient electro-osmotic flow in rotating soft microchannel. *Phys. Fluids* **34** (8), 082023.
- GHOSAL, S. 2002 Lubrication theory for electro-osmotic flow in a microfluidic channel of slowly varying cross-section and wall charge. *J. Fluid Mech.* **459**, 103–128.
- GOUY, M. 1910 Sur la constitution de la charge électrique à la surface d'un électrolyte. *J. Phys. Theor. Appl.* **9** (1), 457–468.
- HSIEH, S.S., LIN, H.C. & LIN, C.Y. 2006 Electroosmotic flow velocity measurements in a square microchannel. *Colloid Polym. Sci.* **284**, 1275–1286.
- KAUSHIK, P., MANDAL, S. & CHAKRABORTY, S. 2017a Transient electroosmosis of a Maxwell fluid in a rotating microchannel. *Electrophoresis* **38** (21), 2741–2748.
- KAUSHIK, P., MONDAL, P.K. & CHAKRABORTY, S. 2017b Rotational electrohydrodynamics of a non-Newtonian fluid under electrical double-layer phenomenon: the role of lateral confinement. *Microfluid Nanofluid* **21**, 1–16.
- KAUSHIK, P., MONDAL, P.K., KUNDU, P.K. & WONGWISES, S. 2019 Rotating electroosmotic flow through a polyelectrolyte-grafted microchannel: an analytical solution. *Phys. Fluids* **31** (2).
- KEMERY, P.J., STEEHLER, J.K. & BOHN, P.W. 1998 Electric field mediated transport in nanometer diameter channels. *Langmuir* **14** (10), 2884–2889.
- LONG, D., STONE, H.A. & AJDARI, A. 1999 Electroosmotic flows created by surface defects in capillary electrophoresis. *J. Colloid Interface Sci.* **212** (2), 338–349.
- LUNG, F.K. 1966 A new application of Routh–Hurwitz criterion. *Electronic Theses Dissertations* **6432** (1), 14–34.
- LYKLEMA, J. 1995 *Fundamentals of Microfluidics*. Academic Press.
- MADUAR, S.R., BELYAEV, A.V., LOBASKIN, V. & VINOGRADOVA, O.I. 2015 Electrohydrodynamics near hydrophobic surfaces. *Phys. Rev. Lett.* **114** (11), 118301.
- MASLIYAH, J.H. & BHATTACHARJEE, S. 2006 *Electrokinetic and Colloid Transport Phenomena*. John Wiley & Sons.
- MAYUR, M., AMIROUDINE, S. & LASSEUX, D. 2012 Free-surface instability in electro-osmotic flows of ultrathin liquid films. *Phys. Rev. E* **85** (4), 046301.
- MAYUR, M., AMIROUDINE, S., LASSEUX, D. & CHAKRABORTY, S. 2014 Effect of interfacial Maxwell stress on time periodic electro-osmotic flow in a thin liquid film with a flat interface. *Electrophoresis* **35** (5), 670–680.
- MONDAL, P.K., GHOSH, U., BANDOPADHYAY, A., DASGUPTA, D. & CHAKRABORTY, S. 2013 Electric-field-driven contact-line dynamics of two immiscible fluids over chemically patterned surfaces in narrow confinements. *Phys. Rev. E* **88** (2), 023022.
- MURTHY, J.Y. 1987 A numerical simulation of flow, heat and mass transfer in a floating zone at high rotational Reynolds numbers. *J. Cryst. Growth* **83** (1), 23–34.
- NAM, S., CHO, I., HEO, J., LIM, G., BAZANT, M.Z., MOON, D.J., SUNG, G.Y. & KIM, S.J. 2015 Experimental verification of overlimiting current by surface conduction and electro-osmotic flow in microchannels. *Phys. Rev. Lett.* **114** (11), 114501.
- POSNER, J.D. & SANTIAGO, J.G. 2006 Convective instability of electrokinetic flows in a cross-shaped microchannel. *J. Fluid Mech.* **555**, 1–42.

Stability analysis of electro-osmotic flow

- PROBSTEIN, R.F. 2005 *Physicochemical Hydrodynamics: An Introduction*. John Wiley & Sons.
- RAY, B., REDDY, P., BANDYOPADHYAY, D., JOO, S., SHARMA, A., QIAN, S. & BISWAS, G. 2012 Instabilities in free-surface electroosmotic flows. *Theor. Comput. Fluid Dyn.* **26**, 311–318.
- REZA, M. & GUPTA, A.S. 2012 Magneto-hydrodynamic thermal instability in a conducting fluid layer with throughflow. *Intl J. Non-Linear Mech.* **47** (6), 616–625.
- SENGUPTA, S., GHOSH, S., SAHA, S. & CHAKRABORTY, S. 2019 Rotational instabilities in microchannel flows. *Phys. Fluids* **31** (5), 054101.
- SHIVAKUMARA, I.S., LEE, J., VAJRVELU, K. & AKKANAGAMMA, M. 2012 Electrothermal convection in a rotating dielectric fluid layer: effect of velocity and temperature boundary conditions. *Intl J. Heat Mass Transfer* **55** (11–12), 2984–2991.
- SIVA, T., KUMBHAKAR, B., JANGILI, S. & MONDAL, P.K. 2020 Unsteady electro-osmotic flow of couple stress fluid in a rotating microchannel: an analytical solution. *Phys. Fluids* **32** (10), 102013.
- SONG, L., YU, L., ZHOU, Y., ANTAO, A.R., PRABHAKARAN, R. & XUAN, X. 2017 Electrokinetic instability in microchannel ferrofluid/water co-flows. *Sci. Rep.* **7** (1), 46510.
- SURESH, V. & HOMSY, G.M. 2004 Stability of time-modulated electroosmotic flow. *Phys. Fluids* **16** (7), 2349–2356.
- XIE, Y., FU, L., NIEHAUS, T. & JOLY, L. 2020 Liquid–solid slip on charged walls: the dramatic impact of charge distribution. *Phys. Rev. Lett.* **125** (1), 014501.
- ZHANG, M., LASHGARI, I., ZAKI, T.A. & BRANDT, L. 2013 Linear stability analysis of channel flow of viscoelastic Oldroyd-B and FENE-P fluids. *J. Fluid Mech.* **737**, 249–279.
- ZHAO, H. 2010 Electro-osmotic flow over a charged superhydrophobic surface. *Phys. Rev. E* **81** (6), 066314.
- ZHENG, J. & JIAN, Y. 2018 Rotating electroosmotic flow of two-layer fluids through a microparallel channel. *Intl J. Mech. Sci.* **136**, 293–302.